Detection of Seeds in Citrus Using MRI under Motion Conditions and Improvement with Motion Correction

N. HERNANDEZ, P. BARREIRO, M. RUIZ-ALTISENT, J. RUIZ-CABELLO, M. ENCARNACION FERNANDEZ-VALLE

Physical Properties Laboratory, E.T.S.I.A, Polytechnic University of Madrid, Spain
Instituto de Estudios Biofuncionales, Complutense University of Madrid, Madrid, Spain
Centro de Asistencia a la Investigación de Resonancia Magnética Nuclear, Complutense University of Madrid, Madrid, Spain

ABSTRACT: Magnetic resonance imaging (MRI) is studied under an online strategy. Axial FLASH images (780 ms acquisition time) have been analyzed to identify seed-containing oranges conveyed at 50 and 100 mm/s through a 4.7 Tesla spectrometer. Developed algorithms enable an automated identification of oranges with more than one seed, though axial images under motion conditions suffer from significant blurring artifacts. To overcome this hindrance, coronal FLASH images have been acquired (279 ms acquisition time), developing devoted algorithms for motion correction with encouraging results for quality improvement of dynamic images. © 2005 Wiley Periodicals, Inc. Concepts Magn Reson Part B (Magn Reson Engineering) 26B: 000–000, 2005

KEY WORDS: MRI; online; seeds; phase shift; motion correction

INTRODUCTION

The increasing internal quality demand for fruits and vegetables is driving the development of devices that are capable of evaluating different parameters for characterizing such quality (*1–4*). The application of nondestructive techniques under an online strategy (below 1 second/sample) is encouraged by the added value that can be achieved by the product. The capability of the nuclear magnetic resonance (NMR) of giving response to this challenge is relevant as stated by several authors. Zion et al. (*5, 6*) investigated the real-time detection of pits in cherries by MR projections as well as a fast, computerized detection of bruises in apples by MR images; Chen et al. (*7*) demonstrated the feasibility of the FID spectrum for the dynamic evaluation of the maturity stage in avocados; Barreiro et al. (*8*) studied the prospects of the rapid detection of mealiness in apples by NMR relaxometry; and Hernández et al. (*9*) developed a procedure to detect freeze injury in oranges under motion conditions by MRI.

The presence of seeds, especially in mandarin oranges, involves a loss of quality that has a high impact on the prices. This application requires reliable solutions because the size of seeds is a limiting factor. A precedent work developed by Blasco et al. (*10*) under static conditions confirmed the applicability of the MRI technique for seed detection, although the acquisition time (7 s) needs to be shortened for commercial purposes. To reach working velocities close to the optimal ones, some premises arise as necessary: (i)

fruit should be imaged in continuous motion, (ii) the total scan time decrease should minimize the sensitivity to motion as well as to segregate fruit in quality categories, and (iii) the postprocessing algorithm for automatic characterization should be minimally time-consuming.

Among these premises, the second one presents a major limitation as rapid acquisitions such as those using single-shot echo planar imaging require specialized hardware. Radial scan with projection reconstruction is an alternative to 2D Fourier reconstruction and can reduce motion-induced artifacts (*11*). Motion artifacts, which degrade the image, are one of the greatest problems to be solved. This kind of artifact appears because the imaged tissues do not remain in the same location during the time required for the acquisition. Motion can occur during RF pulses, between RF pulses, during sampling, and between phase-encoding steps (*12*). Phase shifts are generated in the acquired k-space that affects the outcome of the image reconstruction and are responsible for ghosting and/or blurring artifacts of the image. The former corresponds to a periodic motion with temporal variations between phase-encoding views (*13*), in a time scale about the recovery time (TR). The latter is a consequence of nonperiodic motions that take place at the time scale equal to or less than the echo time (TE). As the sample motion under online sorting is translational and nonperiodic, the blurring artifact is expected to appear in the MR images, which may occur in any direction and is proportional to the displacement. It causes spatial mismapping of signal from the true location, which leads to a decrease in the edge definition and makes identification of the structures difficult (*13*). Several authors have proposed procedures to correct the motion effect. Some of them employ image-based methods (*14–18*) applicable to conveying conditions where the motion characteristics are extracted from the acquired images without additional information. A second group of researchers apply motion correction either from information previously known (*19*) or extracted from additional acquisitions (*20*). The present study develops a procedure that takes advantage of the two strategies, image based and motion based, to enhance the quality of MR images under motion conditions, allowing a reliable seed detection in citrus fruit.

MATERIAL AND METHODS

Samples

Experimental work was developed on oranges and lemons. Eleven oranges were obtained at a local market and eight lemons were picked from a local orchard. Samples were inspected by MRI before the experiments, identifying eight oranges and four lemons as seed-containing, and three oranges and four lemons as seedless. Samples were maintained at room temperature (23°C) during measurements.

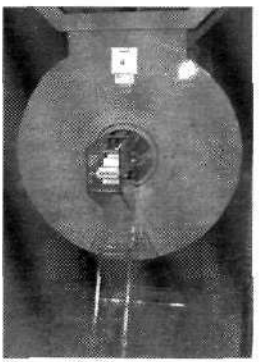

Figure 1 Bruker BIOSPEC 47/40 and conveyor belt.

Two phantoms were used for reference purposes: a sphere filled with doped water (copper sulphate 1% w/w) and a water-filled cube.

MRI Equipment and MRI-Compatible Fruit Conveyor

MRI experiments were performed on a Bruker BIOSPEC 47/40 (Ettlingen, Germany) spectrometer operating at 200 MHz. The bore of the magnet is horizontal, 147 cm long and with a 40 cm diameter reduced to 26 cm when the gradients stack in place. A birdcage coil with an inner diameter of 20 cm was used.

To simulate an online inspection, a special prototype conveyor was designed and built to move the fruits through the spectrometer (see Fig. 1). An electronic device controls the stepper motor that conducts the belt and allows a variable speed drive and bidirectional motion as well as controls the signal acquisition triggering. An electro-optic device detects the fruit as it passes by and delivers a digital signal to the controller to synchronize the MRI signal acquisition with fruit shifts. More details can be found in a previous work (*9*).

MRI Sequences. The phase shift problems arising from the acquisition under motion conditions were bore in mind to select a fast imaging sequence. Short acquisition time leads to a reduction in the displace-

ment and therefore to an improvement in the image quality, and so a fast low angle shot (FLASH) pulse sequence was used.

The major physiological difference between juicy flesh and solid-like seed tissue is the restriction in proton motion. As such, with FLASH T2*-weighted images, seed tissue appears hypointense, whereas flesh tissue appears as bright pixels within the image. The FLASH T2*-weighted sequence parameters used for seed identification in oranges were set to enhance contrast under the restriction of minimum acquisition time: recovery time (TR) 12.2 ms, echo time (TE) 3.8 ms, and flip angle 10 degrees. The field of view (FOV) and the slice thickness used were 12 × 12 cm and 10 mm. The slice thickness was selected to acquire signal from the region with the highest probability of seed presence. Images were collected with 128 × 64 and 128 × 32 acquisition matrix sizes with a total acquisition time of 780 ms and 390 ms respectively. This imaging sequence will hereafter be called type 1.

One type 1 image was obtained from each orange at each run of the belt; the number of acquisitions for signal averaging was set to 1. Three repetitions per fruit were performed to study the repeatability of the measurements. All images were zero-filled to 128 × 128 points before being reconstructed. Images were digitized at 4 bytes. Pulse gains, attenuator, and shimming settings were adjusted with the first sample (selected as representative of the whole set) and were held constant along the experiments.

Oranges used under type 1 images were placed in the belt with their central axis (axis between the poles) along the z direction to obtain axial images displaying the transversal section of the central axis within the middle of the FOV. Within this orientation, seed-containing oranges will have their central axis surrounded by a ring of hypointense region corresponding to seeds.

Synchronization of fruit motion and triggering of signal acquisition for type 1 images makes it possible to locate within the FOV the equatorial area of the fruit while conveyed. This synchronization was set for an orange with average dimensions so that slight FOV location variation may appear for the rest of sampled ones.

For type 1 images, the FOV laid in the plane perpendicular to the motion (xy plane), and superimposition of signals from different slices due to fruit motion led to image blurring.

To acquire signal from a single slice (no slices superimposition), the FOV has to lie in the xz plane; that is to say, coronal images are needed. However, this makes phase shift correction necessary, which may be applied to the k-space lines. This type of image will be called FLASH type 2.

A new experiment was carried out with lemons viewed with type 2 images in order to develop a procedure for phase shift correction. When imaging lemons with type 2 images the acquisition parameters were those of the type 1 ones, with the exception of the FOV orientation, and thus the acquisition times were held (780 ms and 390 ms for each acquisition matrix size). All images were zero filled to 128 × 128 points before being reconstructed. For type 2 images, lemons were placed with their central axis along the y magnet axis. Pulse gains, attenuator, shimming settings, and FOV location were adjusted for a lemon with average dimensions and were held constant.

Type 1 and type 2 were collected under stationary conditions (reference images) and with convey motion through the magnet at 50 and 100 mm/s belt speeds.

Image Processing and Data Analysis for Axial MR Images

Automated Analysis of Orange Images for Seed Detection. Online inspection requires an automated data analysis process that allows unsupervised evaluation of the product. Thus, an initial algorithm was developed using Matlab (The MathWorks, Inc.) to extract several mathematical features (see below) from the magnitude images for the characterization of each sample. Those that best characterized the presence of seeds were selected for further analysis. The algorithm exploits the fact that regions with seeds are displayed as hypointense and it is applied to static and dynamic MR images.

The first step in the algorithm is to automatically select the region of interest (ROI) defined as the fruit portion in which further processing is applied. The background pixels and peel pixels, which have signal intensity below an automatically iterative computed threshold, are not considered for further calculations. On each iteration, threshold intensity is increased and the pixels with signal values above the threshold are identified as part of the ROI. The selected ROI comprises the maximum area surrounded by identified pixels. The end of the iterative process is achieved whenever stabilization in the ROI is reached. More details can be found in a previous work (9).

Once the ROI has been obtained, the low intensity signal regions due to the presence of the central axis and the seeds (if the case) are identified. For the segmentation of such regions the contour Matlab function is used. The following features are calculated from the ROI and hypointense signal region (HIR):

- number of pixels belonging to the ROI;
- number of pixels belonging to the HIR;
- HIR to ROI (seed to tissue) ratio (STR);
- perimeter of the HIR area (P) to extract geometrical information;
- distances from the center of gravity of the HIR to the perimeter points;
- the maximum radius value (R_{max});
- the number of radii higher than the averaged maximum radius of the seed free samples (NR > R_{max});
- the sum of the former radius values (NS > R_{max});
- the number of radii higher than the averaged mean radius of the seed free samples (NR > R_{mean}); and
- the sum of the former radii values (NS > R_{mean}).

These features were correlated at a significance level of 0.05 to establish relations between them and toward the reference measurements. The features with the best correlations were used to join the fruits and to extract the inherent clusters in the studied sample. Cluster analysis was developed using STATISTICA® (StatSoft) according to the Euclidean distances and by applying the Ward's method to minimize the sum of squares (SS) of the hypothetical clusters that can be formed at each step. The inspection of the formed clusters allows assess to the discriminant capability of the used features and to establish the number of groups that can be differentiated by the number of seeds within their samples. Once the number of groups was established, the mean, the standard deviation (SD) and the ratio between the averaged error (averaged SD) and the mean range were obtained as reference measurements for the discrimination (see Fig. 2).

Metrology Measurement of Orange Images. The automatic seed detection procedure has to be consistent and accurate for reliable seed-containing fruits discrimination. Therefore, a study of the repeatability of the features extracted from the MR images was performed.

Repeatability is a measure of the ability of a sensor to reachieve the same response under similar experimental conditions. It was assessed by taking three repetitions of each image and by calculating the average of the standard deviations of computed features.

Appointment of Reference Measurements. Samples were cut in half after MRI for inspection. RGB images of the equatorial fruit section were captured with a digital camera and afterwards seeds within the imaged slice (10 mm thick) were counted.

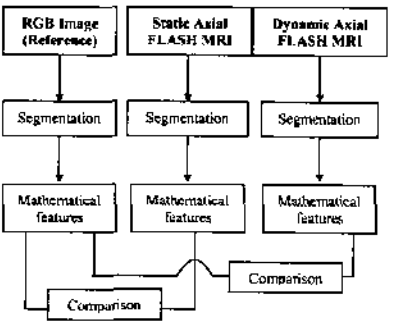

Figure 2 Summary of image processing and data analysis in axial MR images (type 1 images) for seed detection in oranges.

RGB image analysis was applied to segment the area corresponding to the central axis and seeds (if the case). The intensity components in RGB color space (ranging from 0 to 1 and their sum equal to 1) were calculated as indicated in Eqs. [9–11] and used for further segmentation as they are not influenced by the lightness variability.

$$Ir(x, y) = i_r/(i_r + i_g + i_b) \quad [9]$$

$$Ig(x, y) = i_g/(i_r + i_g + i_b) \quad [10]$$

$$Ib(x, y) = i_b/(i_r + i_g + i_b) \quad [11]$$

Here, i_r, i_g, and i_b (ranging from 0 to 255 independently one from another) are the intensities obtained through red, green, and blue filters respectively. The intensity through the blue filter (i_b) was selected to segment the whole tissue without peel, region of interest in RGB images (ROI), whereas the red intensity component (Ir) was selected to segment the seeds and central axis region (SCR), as it enhances the contrast. The histogram segmentation was developed at values of $i_b < 255$ and $i_r < 0.55$.

Image Processing for Coronal MR Images

Computation of Displacement during Lemon MRI. During acquisition, time samples are under continuous motion; therefore, there are view-to-view and intraview displacements. Such displacements can be derived from belt speed × the recovery time for each

pulse sequence. When the conveyor is stable enough, this computation is reliable and can be directly applied for phase shift correction (see below). However, whenever there is a significant lack of homogeneity for the conveyor speed (set with the electronic controller) there will be a significant decrease in the performance of motion correction.

To check the homogeneity of the conveyor speed during type 2 image experiments, navigator (NAV) echoes along the motion belt direction were collected. These special echoes have no phase encoding so that the Fourier transformation will show profiles along the read encoding direction. The sample motion leads to a spatial variation of the profiles from view to view within the field of view.

The most accurate technique to calculate those displacements consists of interleaving the NAV between the views. However, limitations on the acquisition time do not allow such consideration. Thus, a reference displacement was calculated from a sequence of NAV echoes equivalent to the type 2 image (i.e., same data array size, pulse program, and gradient program) with no phase encoding gradient. The reference sample was a water-filled cube phantom conveyed through the magnet at the tested belt speeds.

Each NAV echo was Fourier transformed into profile. The modulus values were calculated and normalization was performed. Interpolation was used to obtain subpixel accuracy displacements so that the minimum detected displacement was 0.25 pixels. To extract the view-to-view motion, the correlation and least squares algorithms were applied to the interpolated profiles sets considering each point of them as a point in a space of continuous functions (*21*).

For each interpolated set (64 profiles) collected at 50 mm/s belt speed, the profile in the middle of the k-space was chosen as reference and the rest were shifted pixel by pixel (actually 0.25 × 0.25 pixels). At each iteration step, the distance between the shifted and the reference profile were calculated applying the distance functions for the correlation method [1] and the least square method [2] extracted from (*21*):

AQ: 8

$$c(d) = -2 \cdot \sum_{x=w/2}^{w/2-1} [S_d(x) - s_r(x)] \cdot s_r(x) \qquad [1]$$

$$I(d) = \sum_{x=w/2}^{w/2-1} |s_d(x) - s_r(x)|^2 \qquad [2]$$

where $s_d(x)$ is the profile shifted a displacement d, $s_r(x)$ is the reference profile, and w is the swept points within the navigator profiles (512 points).

The d value that gives the minimum distance is extracted for each method. Then, the distance between consecutive profiles (Δx) is calculated and averaged for the whole profiles set being analyzed. Slight discontinuity problems arising from the belt advance lead to the need of individually adjust the reference displacement for each image. The entropy minimization (*17*) was used as auto correction (this criterion will be described in the following section).

Motion Correction in Lemon Images. According to the Fourier shift theorem (*22*), if a function $f(x)$ has a Fourier transform $F(s)$ when it is shifted, an amount Δx the Fourier transform of $f(x-\Delta x)$, $F'(s)$, is $e^{-i2\pi\Delta x s}F(s)$. This displacement does not change the amplitude but rather the phase of the complex points in the sampled echoes (*20*). Note that $F(s)$ is a complex number $(R + iI)$ and so is $F'(s)$ $(R + iI')$ and that in order to obtain the former the later is multiplied by the inverse of the phase factor, $e^{-i2\pi\Delta x s}$ (*23*). The phase shift was calculated by Eq. [3] where the center of the echo is used as the reference point and the immediate earlier and latter points are rotated negatively and positively respectively.

$$\Delta\Phi_x = 2\pi \cdot \Delta x \cdot \left[s - \binom{N_x - 1}{2} \right] \cdot \frac{1}{N_x} \qquad [3]$$

Here, N_x is the number of acquired points in the echo (128 points), and s is the point within the echo. For each phase-encoding step, $\Delta\Phi_x$ is multiplied by the corresponding index (ranging from −31 to +32). As during the echo acquisition, the sample does not stop moving, the phase shift due to the intraview motion had also to be bore in mind. It is calculated with the sampling time, i.e, dwell time (20 μs) and the repetition time by the following equation:

$$\Delta\Phi_{ic} = \frac{2\pi \cdot \Delta x \cdot DwellTime}{TR \cdot N_x} \qquad [4]$$

Once the total phase shift, $\Delta\Phi$, at each point is calculated as the sum of $\Delta\Phi_x$ and $\Delta\Phi_{ic}$, the real and imaginary components of the echoes complex points are corrected individually (*20*). The following expressions were applied:

$$R_c = R' \cdot \cos(\Delta\Phi) - I' \cdot \sin(\Delta\Phi) \qquad [5]$$

$$I_c = R' \cdot \sin(\Delta\Phi) + I' \cdot \cos(\Delta\Phi) \qquad [6]$$

where R' and I' are the originally acquired real and imaginary components and R_c and I_c are the corre-

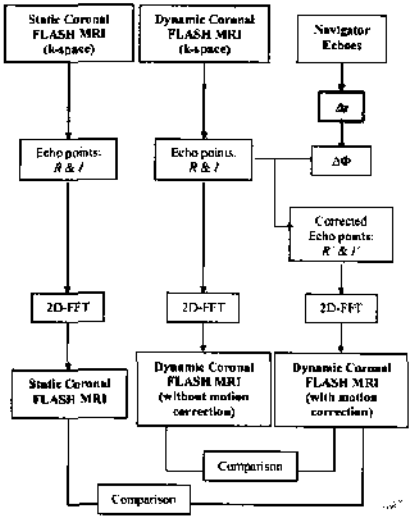

Figure 3 Summary of motion correction procedure for coronal images (type 1 images).

sponding corrected values. For the correction the middle echo was taken as reference so that the image would appear as static at that reference position (*20*). The corrected data were zero filled to 128 × 128 and a two-dimensional Fourier transform were performed to obtain the images (see Fig. 3).

As was previously stated the displacement between echoes, Δx, obtained from the NAV echoes has to be adjusted for each image. The entropy minimization criterion (*17*) was used to select the displacement that better corrected the image. Though the motion artifact is seen as ghosting and/or blurring of the image, the entropy minimization increases the number of dark pixels in the image favoring high contrast (*17*) and facilitating the correction adjustment. As the belt speed is not absolutely constant, to find the displacement that minimized the entropy of the image, the Δx obtained with the phantom was automatically ranged from the calculated value minus 0.03 to the calculated value plus 0.03 varying 0.01 each step. This range was selected after computing the average variation of Δx between homologous experiments. The entropy was calculated at each step with the following expression:

$$E = -\sum_{j=1}^{s} \frac{B_j}{B_{max}} \ln\left(\frac{B_j}{B_{max}}\right) \qquad [7]$$

where s is the number of image pixels (128 × 128), B_j (pixel "brightness") is the modulus of the complex value of the j^{th} image pixel and B_{max} (*8*), which remains invariant under translational motion, is the largest possible pixel brightness obtained if all the image energy were in one pixel (*17*).

$$B_{max} = \sqrt{\sum_{j=1}^{s} B_j^2} \qquad [8]$$

The Δx value that gave the minimum E was selected to correct the motion and thus to obtain the corresponding image.

Quality Evaluation of Lemon Images after Motion Correction The images obtained under motion conditions from the two different slice positions (i.e., *xy* plane and *xz* plane) were evaluated to establish which kind offered the best quality for the subsequent segmentation. In static images of citrus with seeds, the histogram of the selected ROI shows clearly two populations of pixels, those corresponding to the peel, seeds, and central axis region (lower intensity signal) and those of the flesh region (higher intensity signal). When image is blurred, peaks are broadened and even overlap. It leads to a variation in the lower percentiles of the histograms. An analysis of variance (ANOVA) at 1% and 5% significance levels was applied to the lower quartile (as it mainly represents the pixels belonging to seed) of the ROIs in the MR images under static and dynamic conditions. This study was developed to assess differences between the histograms of the static images and their corresponding images acquired under dynamic conditions.

RESULTS AND DISCUSSION

Oranges sorted as seed-containing with MRI were confirmed as so by destructive internal inspection. For all oranges, the number of seeds ranged from 0 to 19 within the whole fruit and from 0 to 10 within the slice imaged by MRI. When the equatorial section and the MR images were visually compared, the correspondence between the seed location and the low signal regions in these images could be revealed. RGB segmentation of fruits cross-section also revealed such correspondence (Figs. 4 and 5). Table 1

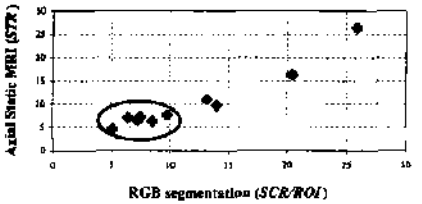

Figure 4 Comparison of automated MRI segmentation (nondestructive) under static conditions and RGB segmentation (destructive). Values of seedless oranges and oranges containing one seed are within the ellipse.

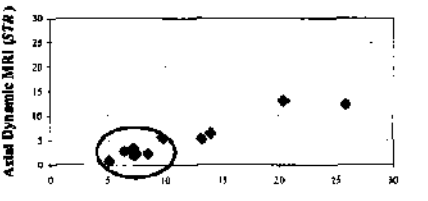

Figure 5 Comparison of automated MRI segmentation (nondestructive) under dynamic conditions and RGB segmentation (destructive). Values of seedless oranges and oranges containing one seed are within the ellipse.

shows the number of seeds within the imaged slice and the ratio SCR/ROI obtained with RGB segmentation.

Seed Detection in Axial MR Images

Axial images under motion conditions showed blurring due to the superimposition of signal arising from new tissue reaching the spatial position of the selected field of view during the acquisition time. As expected, the higher belt speed and/or the lower acquisition matrix size the higher the problems concerning blurring artifacts. However, the contrast between the flesh signal and the seeds and central axis tissue was enough to allow a reliable segmentation when samples were conveyed through the magnet at 50 mm/s belt speed with 128 × 64 acquisition matrix size. F6 Figure 6 shows some examples of seed-free oranges and oranges containing seeds.

The algorithm developed to extract mathematical features for seed detection was applied to the static axial MR images and the axial MR images under motion conditions. These features were linearly correlated to the SCR/ROI ratio extracted from the RGB T2 images (see Table 2).

As shown in Table 2, most of the MRI features show high correlation coefficients with the RGB reference measurement. The ratio of hypointense signal (HJR) tissue with regard to the region of interest (STR) and the perimeter (P) of the HJR are the best correlated. The high r values suggest that the segmentation in MR images is reliable. This result is consistent under static and dynamic conditions, so these parameters were selected to develop further analysis.

The STR and P values corresponding to three repetitions per orange were considered as individual samples and used for unsupervised orange clustering. This analysis grouped the oranges into two main clusters, containing oranges with 0 or 1 seed (cluster 1) and fruits containing more than 1 seed (cluster 2), ranging from 2 to 10. Although it is possible to subdivide the cluster with high seed-content, it is difficult to differentiate seedless oranges from those with a single seed because of the variability in size of the central axis area (see Figs. 4 and 5). The cluster analysis provides the mean and the standard deviation (SD) for each cluster and the ratio between the averaged error (averaged SD) and the range (cluster 2 mean minus cluster 1 mean). These data are summarized in Table 3. T3

Table 3 shows the results of the clustering procedure corresponding to features from axial static MR images compared with those of dynamic axial MR images. The average difference between clusters is always lower for the dynamic MR images than for

Table I Number of Seeds within the Imaged Slice and Characterization of RGB Segmentation

	Oranges without Seeds			Oranges with Seeds							
(SCR[a]/ROI[b])	1	2	3	4	5	6	7	8	9	10	11
Number of seeds	0	0	0	1	1	1	1	2	3	7	10
SCR[a]/ROI[b] (%)	6.4	7.2	7.5	8.5	9.8	7.3	6.2	13.2	14.0	20.4	25.9

[a] SCR = seed and central axis region in RGB images (number of pixels).
[b] ROI = region of interest; entire tissue area in RGB images (number of pixels).

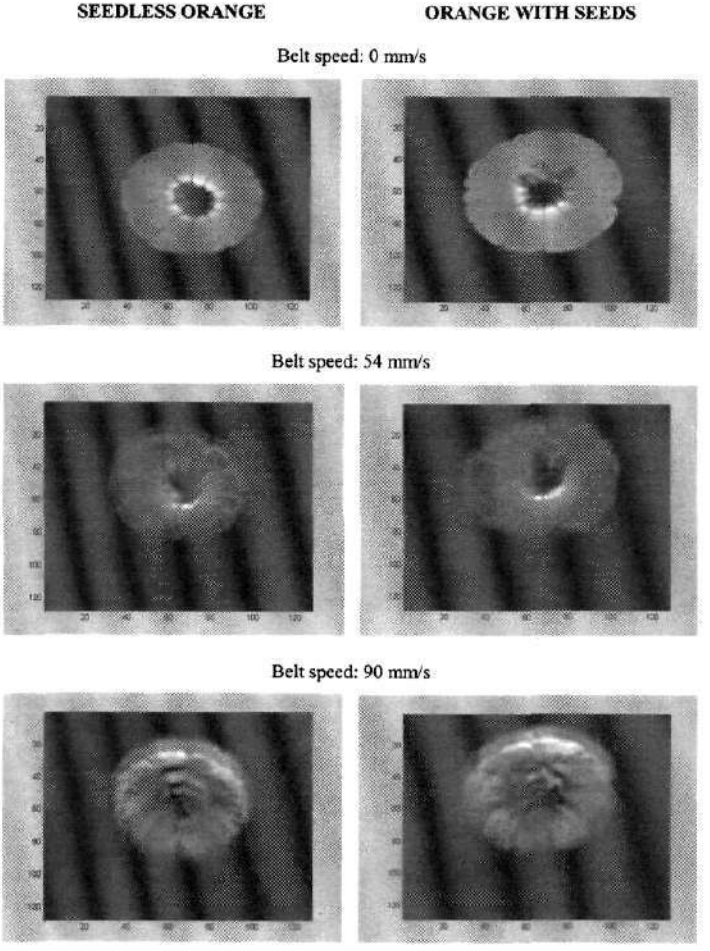

Figure 6 MRI examples (type 1) of seedless oranges and oranges containing seeds at different belt speeds.

static MR images as a result of the superimposition of signal from the different tissues measured during motion. In cluster 1 (0 or 1 seed), the SD does not vary significantly; in cluster 2 (2–10 seeds), the decrement in the SD under dynamic conditions shows that differences between oranges became less clear as STR and P values are more homogeneous within the cluster. The reduction in SD/range ratio suggests that distance between clusters also decreases under dynamic conditions as a result of blurring. When STR computed from MR images is compared with that computed from RGB images (features not shown), the major similarities are seen under static conditions, as the image quality is higher (see Fig. 4).

Table 2 Linear Correlation Coefficient between Reference Measurements (SCR/ROI at RGB Image) and MRI Features

	Linear Correlation Coefficient MRI-RGB (r)						
	STR	P	$4\pi HIR/P^2$	$NR > R_{max}$	$S > R_{max}$	$NR > R_{mean}$	$S > R_{mean}$
Static axial MRI	**0.96**	**0.97**	**−0.82**	0.63	0.54	0.9	**0.88**
Dynamic axial MRI	**0.95**	**0.97**	0.62	**0.77**	**0.81**	**0.82**	**0.82**

Note: Bold type indicates significant correlations.

SCR = seed and central axis region in RGB images (in number of pixels); ROI = region of interest in RGB images (in number of pixels); HIR = hypointense signal region (in number of pixels); STR = HIR to ROI (in MR images) ratio; P = perimeter of the HIR (in number of pixels); $NR > R_{max}$ = number of radii higher than the averaged maximum radius of the seedless samples; $S > R_{max}$ = sum of the former radii values; $NR > R_{mean}$ = number of radii higher than the averaged mean radius of the seedless samples; and $S > R_{mean}$ = sum of the former radii values.

To study the robustness of mathematical features, the repeatability error of the STR and P was computed. Table 4 shows that these parameters are less consistent when fruit is conveying through the magnet as the averaged SD has higher values than those under static conditions. The repeatability error is observed to increase when the number of seeds becomes greater (cluster 2).

These results show that STR is the best MRI feature for seed characterization as it leads to a higher distance between clusters and has better repeatability results.

As expected, the better the image quality the better the repeatability and discrimination. Thus, for application purposes, it is necessary to reduce the blurring in the images by acquiring them in such a way that the imaged tissue does not change along the acquisition duration to ensure that there is no signal superimposition, i.e. selecting the slice to image laying on the *xz* plane (coronal image). Therefore, it was necessary to develop an algorithm aimed at correcting the phase shift in the k-space lines caused by the change in the slice location within the FOV during acquisition. This procedure had to be time efficient as well.

Relevant recent work has been done in fruit-grading lines toward ensuring fruit orientation, which is a major restriction for some innovative quality-sensing techniques. Therefore, state of the art can be used for large-scale applications (*24*, *25*).

Table 3 Statistics of Clusters Generated with MRI Features

	Axial Images (Type 1)			
	Static Conditions		Dynamic Conditions	
	Cluster 1	Cluster 2	Cluster 1	Cluster 2
STR (%)				
Mean	6.6	16	2.8	9.7
SD	0.9	6.9	1.4	3.8
SD/range (%)	41.5		37.7	
P (no. of pixels)				
Mean	70	209	45	107
SD	14	91.4	15.6	9.2
SD/range (%)	38		20	

SD = standard deviation; STR = seed tissue to region of interest ratio; P = seed tissue perimeter.

Motion Correction in Coronal MR Images for Seed Detection Improvement

The NAV echoes of the phantom verified that the conveyor used for the experiments presents high stability for belt speed, allowing a successful determination of the displacement (Δx) during signal acquisition. However, controller speed was revealed to be 54 ± 0.8 mm/s and 90 ± 3.9 mm/s instead of 50 and 100 mm/s. Figure 7 illustrates the relative position of the profiles (from 1 to 64) obtained by Fourier transforming the NAV echoes acquired at 54 mm/s belt speed. The correlation and the least square methods

Table 4 Repeatability Error of the Computed MRI Features under Static and Dynamic Axial Sequences (50 mm/s belt speed)

	Axial Images (Type 1)			
	Static Conditions		Dynamic Conditions	
	Cluster 1	Cluster 2	Cluster 1	Cluster 2
STR (%)	0.1	0.3	0.3	1
P (no. of pixels)	1	3	6	8

STR = seed tissue to region of interest ratio; P = seed tissue perimeter.

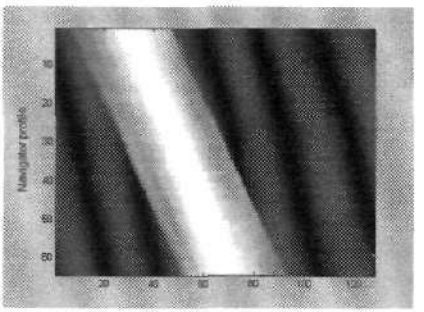

Figure 7 Navigator echoes (NAV) used for type 2 images to address the relative position of the profiles obtained for a phantom during motion at 54 mm/s.

both computed the same displacement between consecutive profiles in all the studied cases.

The average displacements between consecutive profiles were obtained for type 2 images at 54 mm/s as 0.70 pixels and at 90 mm/s as 1.15 pixels. The repeatability error was 0.01 pixels and 0.05 pixels respectively. Note that subpixel displacement can be addressed because of interpolation and was used for accurate phase shift correction.

The reference displacement was adjusted for each reconstructed 128 × 128 matrix size images. Figure 8 illustrates an example of motion correction. The result of the correction is qualitatively impressive, though some objective measures of the quality increase were performed.

Figure 9 shows the histograms of axial and coronal MR images: static axial (up/left), dynamic axial (up/right), static coronal (down/left), and dynamic coronal with motion correction (down/right). Visually, it can be appreciated that there is a reliable correspondence between histograms of coronal images. An ANOVA (Table 5) shows that there is a significant difference in the mean intensity signal value at the 1% and 5 % significance levels for both sorts of images. However, lower quartile is invariant in the coronal images with motion correction with regard to static coronal images, whereas it is significantly different between static and dynamic axial images.

CONCLUSIONS

FLASH imaging sequence is a suitable technique for the online detection of seeds in citrus. Encouraging results have been achieved when oranges were axially imaged under static conditions and while moving at 54 mm/s belt speed. At higher speeds, loss in quality of axial images does not allow seed identification.

An algorithm has been successfully developed for the discrimination of oranges with more than one seed. However, due to the variability in the thickness and the geometry of the central axis, it is not possible to distinguish seedless oranges from single-seed fruits—a major criterion for quality and prize devaluation.

The percentage of hypointense tissue in relation to the whole tissue (STR) is the most reliable feature for seed identification. These results are greatly influenced by the image quality. As a result, it is impera-

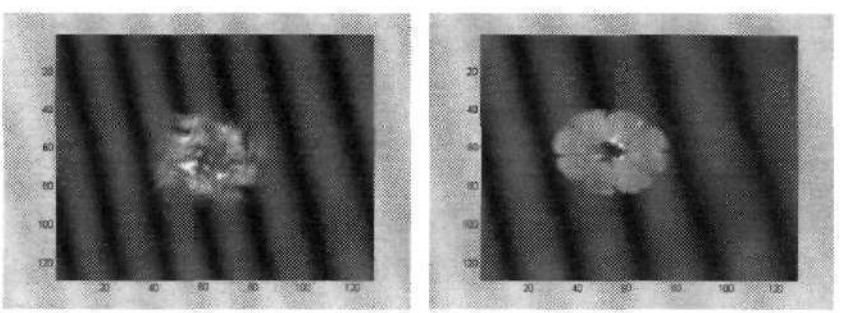

Figure 8 Examples of coronal MR images without and with motion correction (left and right respectively.)

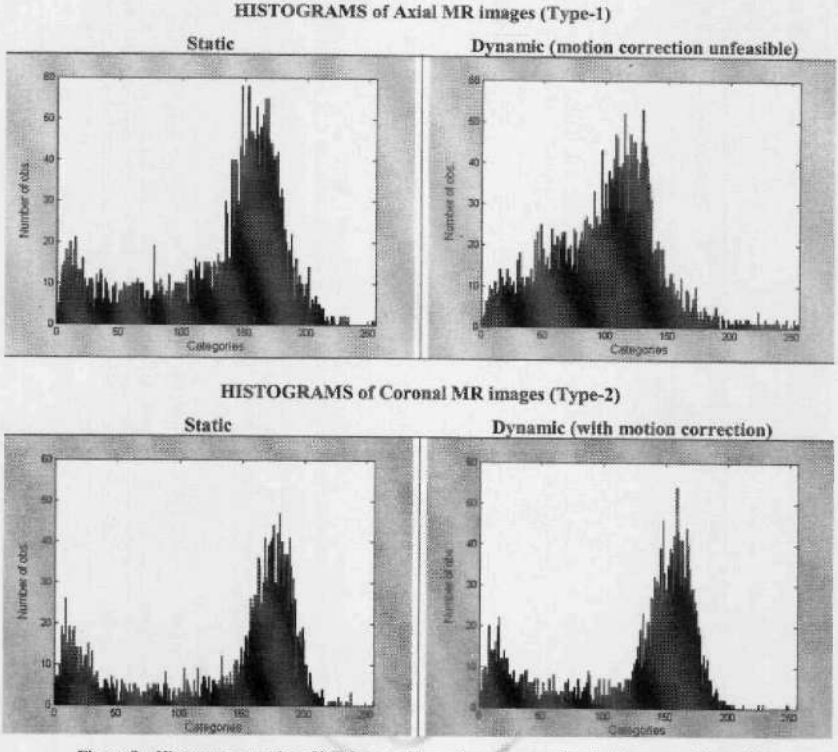

Figure 9 Histogram examples of MR images. Upper line corresponds to the histogram of an axial image under static (left) and dynamic (right) conditions. Lower line corresponds to the histogram of a coronal image under static (left) and dynamic conditions (54 mm/s belt speed) with motion correction (right).

Table 5 Results of ANOVA (1% and 5% Significance Level) for the Histogram Features

	Axial Images (Type 1)			
	Static	Dynamic	F	*p*
Mean	9.56E+08	6.80E+08	41.415	**
Lower quartile	8.70E+08	5.24E+08	34.9096	**
	Coronal Images (Type 2)			
	Static	Dynamic	F	*p*
Mean	1.48E+06	1.32E+06	20.348	**
Lower quartile	1.23E+06	1.16E+06	0.5253	n.s.

* = significance at 1%; n.s. = no significance.

tive to reduce the motion artifacts displayed in the images.

The acquisition of coronal images and the development of a low time-consuming motion correction procedure is the first step in the achievement of high-quality online MR images and will be used in further research for the identification of single-seed fruits.

ACKNOWLEDGMENTS

We thank the Spanish Science and Technology Ministry for financing the project OPTIFRUT (AGL 2001-3792-C02-01).